Journal of Materials Chemistry A

PAPER

View Article Online
View Journal | View Issue

Cite this: J. Mater. Chem. A, 2019, 7, 2787

Ultratough nacre-inspired epoxy–graphene composites with shape memory properties†

Chuanjin Huang,‡[a] Jingsong Peng,‡[a] Yiren Cheng,[a] Qian Zhao,[b] Yi Du,[cd] Shixue Dou,[cd] Antoni P. Tomsia,[a] Hanoch Daniel Wagner,[e] Lei Jiang[ad] and Qunfeng Cheng *[ad]

Shape memory polymers are widely used in industrial applications. Despite extensive and continuous research studies, it is still a great challenge to improve the mechanical properties without affecting their shape memory properties. One approach to improving them is to seek inspiration from natural materials that exhibit superior performance and provide an infinite source of design guidelines. Inspired by the hierarchical architecture of nacre, we have prepared nacre-like shape memory epoxy–graphene composites *via* freeze-casting, a technique to create lamellar materials with complex hierarchical microstructures. Perpendicular to the lamellar direction, the fracture toughness of our composites is ~2.5 times that of the epoxy matrix, due to the synergy of extrinsic toughening mechanisms combining crack deflection, crack branching, crack bridging, and friction between the layered platelets. We achieved high damage-tolerance in our composites by having some degree of plasticity to relax stresses in an epoxy layer. The shape memory properties can be activated using external heating. Due to the electrical conductivity of graphene, we have also achieved electro-active shape memory composites. Our approach suggests an avenue for producing bioinspired shape memory composites with good mechanical and multi-functional properties by utilizing the design principles and strengthening/toughening mechanisms active in nacre and other biological materials.

Received 7th November 2018
Accepted 7th January 2019

DOI: 10.1039/c8ta10725d

rsc.li/materials-a

Shape memory polymers (SMPs) are known as a unique class of smart materials that can be deformed or fixed into temporary shapes and then recover to their permanent shapes upon exposure to certain stimuli, such as temperature,[1,2] light,[3] electricity,[4,5] and magnetic fields.[6] These stimuli-responsive polymers have drawn attention for decades owing to their potential for application in many fields, including aerospace,[7] medical devices,[1] robotics,[8] and others. Research into varieties of SMPs has grown rapidly in recent years, and many SMPs have been discovered, such as dual-shape polymers,[9] triple-shape polymers,[10] reversible shape memory polymers,[11] and healable performance polymers.[12] However, these studies mainly focused on the design of novel shape memory properties, and the improving mechanical properties of SMPs with a homogenous structure were restricted by mixing nanofillers into the matrix. It is worth noting that the mechanical properties of SMPs have not been addressed from the perspective of designing structures of materials in the scientific literature. Optimizing the combination of mechanical and functional performance of SMPs remains a major challenge.

Natural materials, such as nacre in seashells, wood, and skin, to name a few, show exceptional mechanical and/or self-healing properties. For example, nacre, which is composed of 95 vol% inorganic $CaCO_3$ and 5 vol% biopolymers, has excellent fracture toughness, which in energy terms is ~3000 times higher than that of its constituents. Nacre is essentially a laminated composite, with a brick-and-mortar microstructure designed for exceptional damage tolerance.[13] Nacre provides a gold standard for designing and fabricating novel materials.[14] During the last few decades, many methods, such as layer-by-layer assembly,[15–18] infiltration,[19–21] evaporation,[22,23] and electrophoretic deposition,[24–26] have been developed to fabricate bioinspired structural materials, but these techniques are mainly focused on producing films, and are time-consuming and size-limiting. Other techniques, such as the extrusion and roll method[27] and 3D printing,[28,29] which are employed to

[a]Key Laboratory of Bio-inspired Smart Interfacial Science and Technology of Ministry of Education, School of Chemistry, Beijing Advanced Innovation Center for Biomedical Engineering, Beihang University, Beijing 100191, P. R. China. E-mail: cheng@buaa.edu.cn

[b]State Key Laboratory of Chemical Engineering, College of Chemical and Biological Engineering, Zhejiang University, Hangzhou 310027, P. R. China

[c]Institute for Superconducting and Electronic Materials, Australian Institute for Innovative Materials, University of Wollongong, Wollongong, New South Wales 2500, Australia

[d]BUAA-UOW Joint Research Centre, Beihang University, Beijing 100191, China

[e]Department of Materials & Interfaces, Weizmann Institute of Science, Rehovot 76100, Israel

† Electronic supplementary information (ESI) available. See DOI: 10.1039/c8ta10725d

‡ These two authors contributed equally to this work.

engineer bulk materials, cannot control the microstructure of these composites precisely.

A more promising recent technique to fabricate nacre-like bulk materials is freeze-casting, also called ice-templating.[30,31] During controlled freezing of powder suspensions in water, the micro/nano-materials are expelled and concentrated in the gap between the ice crystals, forming porous lamellar structures.[32,33] Deville *et al.*[34] pioneered the fabrication of nacre-inspired lamellar alumina (Al_2O_3) scaffolds by unidirectional freeze-casting. Munch *et al.*[35] further extended the technique by producing an Al_2O_3–polymethyl methacrylate (PMMA) nacre-inspired brick-and-mortar structure with outstanding mechanical properties. The resulting properties of the composites show strength comparable to that of Al_2O_3 (225 MPa) but their toughness is an order of magnitude larger, with a fracture toughness of above 30 MPa $m^{1/2}$. In addition to ceramic particles or platelets,[36–38] polymers or fibers, such as chitosan (CS),[39] silk fibroin,[40] silica (SiO_2) fibers,[41] and silicon carbide (SiC) fibers,[42] can also be used to create structural materials by freeze-casting. Graphene, with its exceptional mechanical properties and high conductivity, is an ideal candidate for constructing high performance structural materials.[43–46] Freeze-casting is frequently used to produce complex hierarchical structures and composites with superior properties by incorporating graphene. By mimicking the hierarchical structure of cork, Qiu *et al.*[47] fabricated ultralight graphene-based cellular monoliths by unidirectional freeze-casting. The foams are superelastic with exceptionally low density. An elegant combination of freeze-casting, infiltration, and spark plasma sintering to fabricate ceramic–graphene composites was recently reported by Picot *et al.*;[48] thus, the obtained graphene networks display self-monitoring properties. However, these as-prepared graphene foams needed the assistance of additives, such as L-ascorbic acid (L-AA), PVA, and CS. Zhang *et al.*[49] obtained a large-scale aligned graphene oxide (GO) membrane by ethanol-assisted freeze-casting without any additives. After thermal reduction and O_2-plasma treatment, the graphene membrane shows highly efficient solar thermal generation.

Herein, we describe our method to fabricate GO scaffolds *via* a tetrahydrofuran (THF)-assisted bidirectional freeze-casting technique. Our scaffolds show an anisotropic large-scale lamellar structure. Using thermal reduction to recover the conductivity of graphene, the volume of the as-obtained rGO scaffolds exhibited slight shrinkage and reduction in weight due to the removal of oxygen-containing functional groups. Shape memory epoxy (EP)[50] was infiltrated into the rGO scaffolds, forming, after curing, nacre-like shape memory epoxy–graphene (E–G) composites. The resultant composites show a good improvement of the fracture toughness of the EP matrix (~2.5 times) and exhibit a shape memory effect with thermal or electrical stimuli. Our approach suggests an avenue for producing bioinspired shape memory composites with good mechanical and multi-functional properties by utilizing the design principles and strengthening/toughening mechanisms active in nacre and other biological materials.

Results and discussion

Designing the architecture of E–G composites is the critical step for constructing novel structural materials. Modified bidirectional freeze-casting was applied to assemble the hierarchical layered structure ranging from nano/microscopic to macroscopic. Pre-fabricated GO was dispersed in deionized water to obtain homogeneous 9 mg ml^{-1} and 15 mg ml^{-1} GO contents in aqueous suspensions *via* ultrasonication, as shown in Fig. 1a and S1.† Subsequently, these suspensions were frozen using the bidirectional freeze-casting technique. During freezing, the ice crystals grew along dual temperature gradients, expelling the GO to concentrate between the gaps of layered ice. THF was used as the anti-freeze agent, which decreased the freezing rate and dramatically affected the crystallization behavior of the ice with hydrogen bonds,[51,52] thus contributing to the formation of a large-scale aligned structure (see Fig. 1b).

After removal of the ice by freeze drying, the lamellar GO scaffold had enough strength for easy handling (Fig. 1c). There are many bridges between adjacent layers, endowing the GO scaffold with integrity and strength (Fig. S2a†). To recover the conductivity of graphene, the GO scaffold was sintered at 800 °C for 1 hour in nitrogen. The color of the scaffold changed from dark yellow to grey, as shown in Fig. 1d. The structure of the rGO scaffold exhibited a large-scale lamellar morphology, while the space between the layers was significantly reduced (Fig. S2b†). To achieve multi-functional composites, shape memory EP was vacuum infiltrated into the rGO scaffold. After curing at 130 °C for 2 hours, nacre-like shape memory E–G composites were obtained (Fig. 1e). GO scaffolds produced with 9 mg ml^{-1} and 15 mg ml^{-1} GO suspensions were named as GO-I and GO-II, respectively. Corresponding to the GO scaffolds, the rGO scaffolds and shape memory E–G composites were denoted as rGO-I and rGO-II, and E–G-I and E–G-II, respectively. For a control sample, an rGO powder with the same content as the rGO-II scaffold in E–G-II (~0.60 wt%) was added to the EP, forming homogeneous composites by mixing and curing. The control sample is denoted as E–G–H.

The scanning electron microscope (SEM) images of scaffolds and composites display an anisotropic structure, as shown in Fig. 2. The cross-section of the GO scaffold shows a lamellar architecture, and the side of the scaffold is composed of large lamellae with asperities (see Fig. 2a). The GO scaffold shows a 3D interconnected network having a stable structure. The as-obtained GO scaffolds do not contain any additives or reduced agents, such as PVA, sodium carboxymethyl cellulose (SCMC), sodium alginate (SA), or L-AA. Due to the oxygen-containing functional groups grafted to the surface of graphene, the GO scaffolds do not display conductivity.

To recover the conductivity of the graphene, the oxygen groups were removed by heating the scaffolds to 800 °C. After high temperature treatment, the volume of rGO scaffolds decreased to ~80% of their original size, and the weight was reduced to ~50%. X-ray photoelectron spectroscopy (XPS) was used to characterize the content of carbon and oxygen before and after the thermal reduction. Peaks of C1s at 284.8, 286.9,

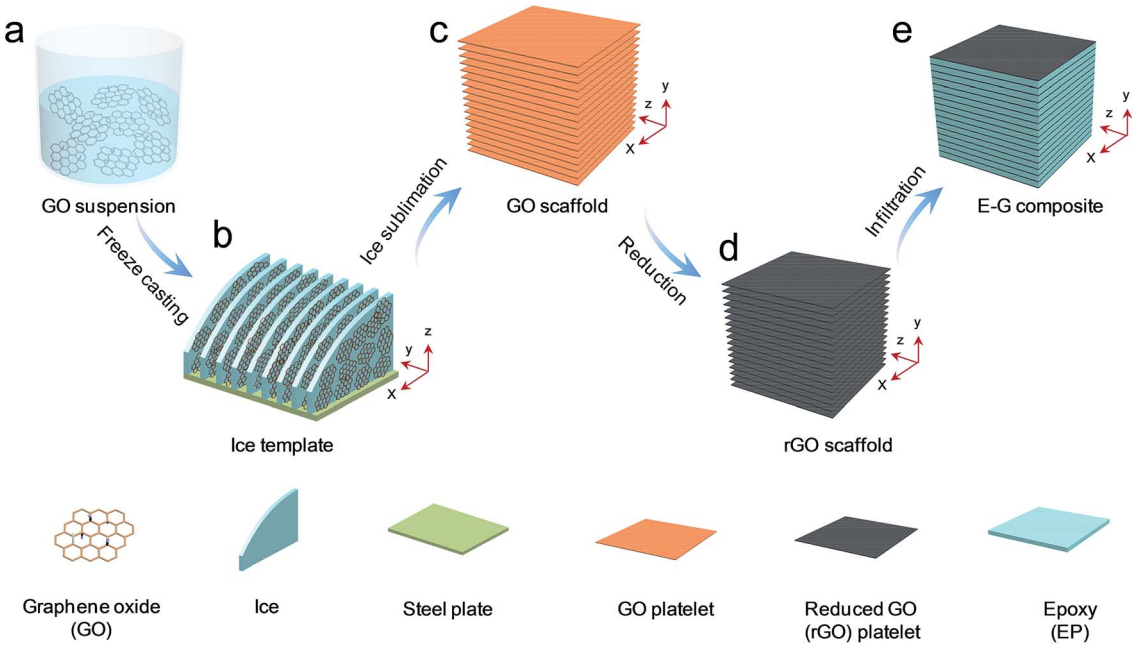

Fig. 1 Schematic of the fabrication of E–G composites: (a) preparation of the GO aqueous suspension with THF and then freezing by bidirectional freeze-casting (b). The lamellar GO scaffold was obtained after freeze drying (c). Subsequently, heating was applied to reduce the GO scaffold, forming an rGO scaffold (d). Finally, the E–G composite was produced by infiltrating with shape memory EP and curing (e).

and 288.7 eV represent C–C, C–O, and C(O)O groups, respectively, in Fig. S3a.† However, there remains only the C–C peak in the spectra, as shown in Fig. S3b,† demonstrating that the oxygen-containing groups have been completely removed from the scaffolds. The morphology of the cross-section clearly shows a lamellar structure with the spacing between layers reduced to ~20–40 μm, as shown in Fig. 2b. The rGO scaffolds exhibited good anisotropy, observed from different angles by SEM (Fig. S4†).

Furthermore, the scaffolds are strong enough to be filled with a second phase to obtain novel composites containing polymer, metal, or ceramic precursors. Shape memory EP was used to construct multi-functional E–G composites *via* vacuum infiltrating EP into the rGO scaffold to remove voids in the process of infiltration. After curing at 130 °C for 2 hours, the resultant E–G composite also shows an anisotropic structure. The cross-section shows rGO layers separated by EP, forming a lamellar composite. The thickness of an EP lamella is ~20–40 μm, and the side image of the composite shows a large EP lamella similar to that of nacre, as shown in Fig. 2c. Therefore, we have emulated the architecture of nacre to create well-ordered lamellar E–G composites. Thermogravimetric analysis

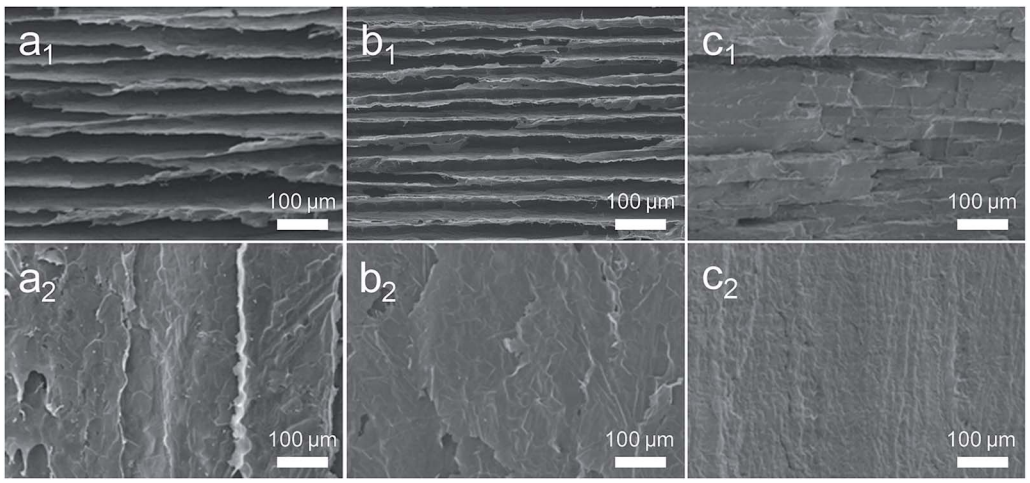

Fig. 2 The microstructures of the scaffolds and E–G-II composite. The GO scaffold shows a lamellar structure at the cross-section (a_1) and a large lamella on the side (a_2). After thermal reduction, the volume of the rGO scaffold shrinks, resulting in reducing of the space between layers (b_1) and the asperities of a lamella (b_2). The as-obtained E–G-II composite maintains a lamellar structure (c_1 and c_2).

(TGA) of EP and nacre-like E–G-II composites indicated that rGO scaffolds did not degrade the EP (Fig. S5†).

The notched specimens were used in three-point bend testing to evaluate the damage tolerance of our materials, with the data shown in Fig. 3a. The force–displacement data for the most part are given here as a means of comparison between each other. The EP force–displacement curve rises and then decreases rapidly (curve 1), resulting in the smooth fracture surface (Fig. S6a†). The maximum force for the E–G–H composite is slightly higher and decreases more slowly than that of EP (curve 2), and there are many stress stripes on the fractured surface (Fig. S6b†). Nacre-like E–G composites required much higher force at failure and further displacement due to the lamellar structure of the composites. Finally, the E–G-II composite is remarkably better than E–G-I (curve 3 and curve 4) because of the more aligned, regular lamellar structure of E–G-II (Fig. S6c and d†). The calculations indicate that the initial fracture toughness (K_{IC}) of these materials rises with the increase of the force at the end of the elastic regime, resulting in the K_{IC} of E–G-II being ~1.5 times higher than that of EP, as shown in Fig. 3b.

To provide an insight into the fracture process, fracture experiments were performed using a SEM. The EP fails catastrophically with no stable crack growth, leading to poor fracture toughness (Fig. 3c). In contrast, the E–G-II composite displays a stable crack growth with a tortuous path. The observed toughening mechanisms are crack deflection, crack branching, crack bridging, and friction when lamellae are pulled out, as shown in Fig. 3d. The modulus (E) of the nacre-like E–G-II composite reaches up to 1.35 GPa perpendicular to the lamellar direction, which is slightly higher than that of EP (Fig. S7†). According to the rising resistance curve (R-curve), the maximum fracture toughness (K_{JC}) of the E–G-II composite perpendicular to the lamellar direction is measured to be 2.63 MPa $m^{1/2}$ within the ASTM limit,[48] which is ~2.5 times higher than that of EP, as shown in Fig. 3e. The critical strain energy release rates (G_{IC}) of EP and E–G-II composites are 743.43 J m^{-2} and 1517.19 J m^{-2}, respectively. More importantly, the work of fracture of the E–G-II composite is 4664.13 J m^{-2}, which is ~6.3 times better than that of EP when taking extrinsic toughness into account.

Fig. 3f shows the advantages of this bioinspired concept for preparing nacre-like composites compared with other traditional EP-based composites. To investigate the increased fracture toughness, the ratio of K_{IC} (composites) and K_{IC} (EP matrix) was used to evaluate the toughening effects of different nanofillers. The EP-based composites prepared by traditional methods including solution mixing and melt mixing are enhanced with common materials such as modified GO,[53–56] functionalized graphene,[57–61] carbon nanofibers (CNFs),[62,63] multiwalled carbon nanotubes (MWNTs),[64] and clay,[65,66] forming homogeneous structures (the corresponding abbreviations of specific nanofillers are listed in Table S1†). However, the ratios of K_{IC} (composites) and K_{IC} (pure EP) of these EP-based composites range from 1.0 to 1.8 and rarely exceed 1.8 because of the poor dispersion and homogeneous structures. Our as-prepared nacre-like E–G composites show significantly higher fracture toughness due to stable crack growth depicted in Fig. 3d; the feature has not been found in other traditional EP-based composites. The ratio of K_{JC} (E–G-II) and K_{IC} (EP) for E–G

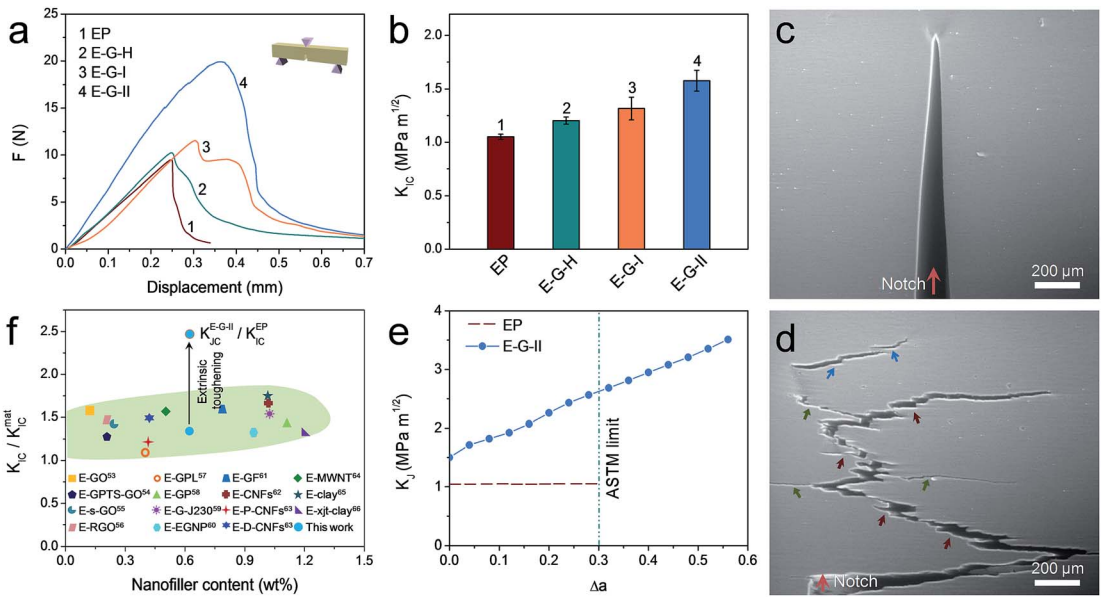

Fig. 3 The fracture toughness and proposed mechanisms of E–G composites: (a) the typical force–displacement curves of EP (curve 1), E–G–H (curve 2), E–G-I (curve 3), and E–G-II (curve 4). (b) K_{IC} of EP, E–G–H, E–G-I and E–G-II. The K_{IC} of nacre-like composites is higher than that of EP and the E–G–H composite. (c) EP shows straight crack growth. (d) The E–G-II composite with the rGO scaffold has stable crack propagation. Proposed fracture mechanisms such as crack deflection (red arrows), crack branching (green arrows), crack bridging (blue arrows), and friction between layers contribute to the superior fracture toughness. (e) The K_{JC} of E–G-II is of the order of 2.63 MPa $m^{1/2}$ in terms of the R-curve. (f) Comparison with the EP-based composites prepared by traditional methods, the nacre-like E–G-II composite shows surpassing fracture toughness when taking extrinsic toughness into account.

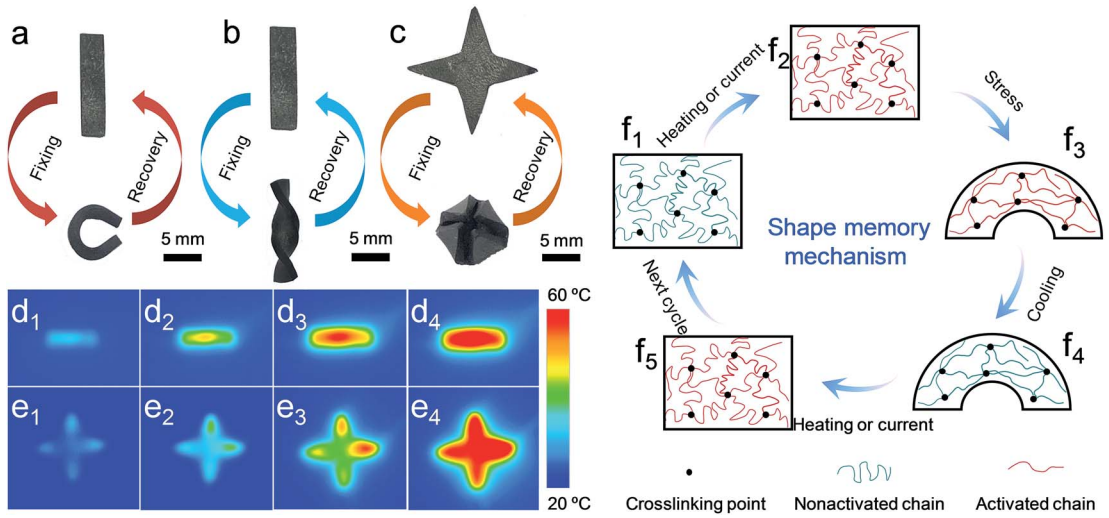

Fig. 4 The shape memory properties of E–G-II composites. The composite can be fixed into various shapes such as a circle (a), twist (b), and fold (c) by heating or exposure to current, forming temporary shapes that can be held below 30 °C. Upon heating or exposure to an appropriate current again, these temporary shapes will recover to their original shapes. (d and e) Infrared thermal images of E–G-II composites. When currents of 5 mA and 10 mA are applied to the composites with the shapes of a strip and star, respectively, the temperatures of these composites increase dramatically, as observed from the infrared images with the elapse of time. (f) The one-way dual-shape memory mechanism of the E–G composite. (f_1) The permanent shape of the E–G composite. (f_2) Non-activated chain segments are activated through heating or exposure to an appropriate current. (f_3) Induced deformation of the E–G composite under stress. (f_4) Cooling this composite and forming a temporary shape without stress. (f_5) Recovering to its permanent shape upon reheating or exposure to current.

composites reaches the value of ~2.5, which is much higher than that of the traditional EP-based composites.

In addition to superior fracture toughness, improved functional performance is also urgently needed in composites for many applications. One of those desired functional properties is shape memory, the ability of a material to recover its original shape with the right stimulus. We created shape memory composites with excellent damage tolerance by infiltrating shape memory EP into our rGO scaffolds. EP is a good insulator, and therefore, our control specimens (E–G–H) show non-conductivity because the nanofillers in the composite are isolated, not connected, and thus cannot form conductive pathways. Nacre-like composites with a 3D interconnected network can demonstrate excellent electrical conductivity even when the content of the nanofillers is only 0.60 wt%. The conductivity of E–G-II along the lamellar direction is ~55 times better than that of E–G-I due to the higher content of rGO. It is also ~6 times better as compared to its conductivity perpendicular to the lamellar direction (Fig. S8†). The continuous graphene network does not affect the shape memory properties of E–G-II composites. Instead, it provides an electro-active shape memory path. In other words, the shape recovery behavior of our composites can also be triggered by electrical current.

Consequently, E–G-II composites can be molded into various shapes, such as a circle (Fig. 4a), twist (Fig. 4b), and fold, (Fig. 4c) using heating or current stimuli under deformation stress, forming temporary shapes, and then recover to their permanent shapes upon the same stimuli (Fig. S9†). We utilized the infrared thermal images to investigate the mechanism of driving the shape memory effect by electricity. The results show that the temperature of a strip sample increases in one minute when electrical current is applied (5 mA), which is recorded by the infrared images (Fig. 4d). The composite with the shape of a star also shows an excellent electro-thermal effect using a constant current of 10 mA within a few minutes (Fig. 4e). Once the internal temperature of these composites reaches glass transition temperature (T_g) (Fig. S10†), the shape recovery behavior would be induced by Joule heating.

The proposed mechanism of a one-way dual-shape memory cycle of such composites is shown in Fig. 4f. The shape memory E–G composites with low cross-linking density and T_g are rigid materials at room temperature (see Fig. $4f_1$). When these composites are exposed to a temperature ($T > T_g$), they become soft elastomers because of the activated molecular chains (Fig. $4f_2$). The external stress can change chain conformation (Fig. $4f_3$), resulting in macroscopic deformation to fix the temporary shape when cooling to room temperature (Fig. $4f_4$). Here, the deformation of the composites is held even after removing the stress owing to the freezing chains locking chain conformation and storage of entropic energy (high energy state). These composites recover their permanent shape when heated or exposed to electrical current, which drives molecular chains back to the lowest energy configuration[8,9] (Fig. $4f_5$). We have investigated the consecutive shape memory cycles in a stress-controlled mode, as shown in Fig. S11.† The results suggest that the strain shift shows little deviation after four cycles, demonstrating exceptional shape fixity and recovery.

Conclusion

In summary, we have synthesized nacre-like shape memory epoxy–graphene composites *via* freeze-casting. Depending on the lamellar structure, the nacre-like shape memory composites

with only ~0.60 wt% rGO content have stable crack extension. During loading, the fracture mechanisms consisting of crack deflection, crack branching, crack bridging, and friction effectively distribute the stress and dissipate much energy. Perpendicular to the lamellar direction, the fracture toughness of nacre-like shape memory composites is ~2.5 times better than that of pure epoxy and superior to those of epoxy-based composites prepared by traditional methods. Furthermore, this kind of nacre-like shape memory composite can be fixed into various shapes including a circle, twist, and fold, and recover its permanent shape when heated or exposed to electrical current. This bioinspired fabrication strategy provides an insightful avenue for producing high performance shape memory composites in the future.

Methods

Materials

GO was synthesized from graphite powder by a modified Hummers' method.[67] THF was purchased from Beijing Chemical Works. Epoxy monomer E44 was purchased from Usolf Chemical Technology Co., Ltd. Poly(propylene glycol) bis(2-aminopropyl ether) (D230) as the curing agent was purchased from Aladdin.

Preparing nacre-like E–G composites

Homogenous GO aqueous suspensions (9 mg ml^{-1} and 15 mg ml^{-1}) were fabricated by ultrasonic treatment (100W, KQ-100DA). THF was added to the GO suspension (a fixed ratio of 1 : 50, v/v) and then stirred for 1 hour. The GO suspension with THF was transferred into a silicone mold (15.0 × 15.0 × 15.0 mm^3) placed on the surface of steel. Liquid nitrogen was utilized to cool one side of the steel plate, forming a temperature gradient. After solidification, the resultant frozen GO suspension was transferred into a freeze dryer (<5 Pa, LGJ-12S) to freeze dry for 2 days. Subsequently, the obtained GO scaffolds were heated at 800 °C for 1 hour in nitrogen (tube furnace, SK-G05125K) to prepare rGO scaffolds. EP monomer E44 and its curing agent (D230) were blended, filled into the rGO scaffold with a vacuum, and then cured at 130 °C for 2 hours (electric drying oven, DH-101) to fabricate shape memory E–G composites.

Characterization

A Quanta 250 SEM was used to observe the microstructure and *in situ* fracture process of samples. TGA was performed on an NETZSCH STA449F3 from 50 °C to 800 °C at a rate of 10 °C min^{-1} in nitrogen. The XPS spectra of GO and rGO scaffold surfaces were acquired using an ESCALAB220i-XL with monochromatic Al-Kα. Differential scanning calorimetry (DSC 6200) was conducted from 10 °C to 130 °C at a heating rate of 10 °C min^{-1}. Dynamic mechanical analyses (DMA Q800) were used to determine the T_g at 1 Hz, 0.2% strain and a heating rate of 3 °C min^{-1}. The consecutive shape memory effect was evaluated with a DMA Q800 at a heating rate of 10 °C min^{-1} and a cooling rate of 5 °C min^{-1} in a controlled force mode.

Beams with a size of 14.0 × 2.5 × 2.5 mm^3 were cut from bulk materials and pre-notched with a water-cooled diamond blade and then sharpened with a razor blade. E–G composites were single-edge notched perpendicular to the lamellar structure. The notches of samples were ~0.45–0.55 of their thickness. Three-point bending (span: 7.75 mm) (SUNS UTM4103) was used to test these samples at a rate of 0.06 mm min^{-1}. Samples (14.0 × 2.5 × 2.5 mm^3) without a notch were painted with a silver paste at both ends for an electrical test using a two-probe method (Agilent E4980A) along and perpendicular to the lamellar direction. The shape memory properties of composites were obtained at a constant temperature heating stage (HP-1515). Infrared thermal images were recorded on a Testo 871.

The mechanical calculation: K_{IC} is calculated using the formulas[68]

$$K_{IC} = \frac{P_{IC} S}{B W^{3/2}} f(a/W)$$

$$f(a/W) = \frac{3(a/W)^{1/2}\left[1.99 - (a/W)(1 - a/W)\left(2.15 - 3.93a/W + (a/W)^2\right)\right]}{2(1 + 2a/W)(1 - a/W)^{3/2}}$$

where P_{IC} is the maximum load of the linear region of the load–displacement curve, S the span, B the width, W the thickness and a the notch, respectively.

K_J is calculated using[39]

$$K_J = [(E J_{pl}/(1 - \nu^2)) + K_{IC}^2]^{1/2}$$

$$J_{pl} = \frac{2A_{pl}}{B(W - a)}$$

Crack extension (Δa) is given as

$$a_n = a_{n-1} + \frac{W - a_{n-1}}{2}\frac{C_n - C_{n-1}}{C_n}$$

$$C_n = u_n/f_n$$

$$\Delta a = a_n - a$$

and G_{IC} is given as[48]

$$G_{IC} = K_{IC}^2(1 - \nu^2)/E$$

where E is the modulus of the composite, ν is Poisson's ratio, and A_{pl} is the area under the force–displacement curve. a_n is the crack length, u_n the displacement, and f_n the force at each point after crack initiation.

Conflicts of interest

There are no conflicts to declare.

Acknowledgements

This work was supported by the Excellent Young Scientist Foundation of NSFC (51522301), the National Natural Science Foundation of China (21875010, 21273017, and 51103004), the Program for New Century Excellent Talents in University (NCET-12-0034), the Fok Ying-Tong Education Foundation (141045), the 111 Project (B14009), the Aeronautical Science Foundation of China (20145251035 and 2015ZF21009), the State Key Laboratory of Organic–Inorganic Composites, Beijing University of Chemical Technology (oic-201701007), the State Key Laboratory for Modification of Chemical Fibers and Polymer Materials, Donghua University (LK1710), the Fundamental Research Funds for the Central Universities (YWF-16-BJ-J-09, YWF-17-BJ-J-33, and YWF-18-BJ-J-13) and the Academic Excellence Foundation of BUAA (20170666) for Ph.D. Students.

References

1 A. Lendlein and R. Langer, *Science*, 2002, **296**, 1673–1676.
2 A. Lendlein and S. KelchAndreas, *Angew. Chem., Int. Ed.*, 2002, **41**, 2034–2057.
3 A. Rose, Z. Zhu, C. F. Madigan, T. M. Swager and V. Bulovic, *Nature*, 2005, **434**, 876–879.
4 H. Koerner, G. Price, N. A. Pearce, M. Alexander and R. A. Vaia, *Nat. Mater.*, 2004, **3**, 115–120.
5 X. Luo and P. T. Mather, *Soft Matter*, 2010, **6**, 2146–2149.
6 J. S. Leng, X. Lan, Y. J. Liu, S. Y. Du, W. M. Huang, N. Liu, S. J. Phee and Q. Yuan, *Appl. Phys. Lett.*, 2008, **92**, 014104.
7 Y. Liu, H. Du, L. Liu and J. Leng, *Smart Mater. Struct.*, 2014, **23**, 023001.
8 B. Jin, H. Song, R. Jiang, J. Song, Q. Zhao and T. Xie, *Sci. Adv.*, 2018, **4**, eaao3865.
9 Q. Zhao, W. Zou, Y. Luo and T. Xie, *Sci. Adv.*, 2016, **2**, e1501297.
10 N. Zheng, J. Hou, Y. Xu, Z. Fang, W. Zou, Q. Zhao and T. Xie, *ACS Macro Lett.*, 2017, **6**, 326–330.
11 M. Behl, K. Kratz, J. Zotzmann, U. Nochel and A. Lendlein, *Adv. Mater.*, 2013, **25**, 4466–4469.
12 Z. Fang, N. Zheng, Q. Zhao and T. Xie, *ACS Appl. Mater. Interfaces*, 2017, **9**, 22077–22082.
13 F. Barthelat, *Science*, 2016, **354**, 32–33.
14 U. G. Wegst, H. Bai, E. Saiz, A. P. Tomsia and R. O. Ritchie, *Nat. Mater.*, 2015, **14**, 23–36.
15 L. J. Bonderer, A. R. Studart and L. J. Gauckler, *Science*, 2008, **319**, 1069–1073.
16 E. R. Kleinfeld and G. S. Ferguson, *Science*, 1994, **265**, 370–373.
17 G. Decher, *Science*, 1997, **227**, 1232–1237.
18 Z. Tang, N. A. Kotov, S. Magonov and B. Ozturk, *Nat. Mater.*, 2003, **2**, 413–418.
19 S. Wan, Y. Li, J. Peng, H. Hu, Q. Cheng and L. Jiang, *ACS Nano*, 2015, **9**, 708–714.
20 A. Walther, I. Bjurhager, J. M. Malho, J. Ruokolainen, L. Berglund and O. Ikkala, *Angew. Chem., Int. Ed.*, 2010, **49**, 6448–6453.
21 S. Gong, W. Cui, Q. Zhang, A. Cao, L. Jiang and Q. Cheng, *ACS Nano*, 2015, **9**, 11568–11573.
22 W. Cui, M. Li, J. Liu, B. Wang, C. Zhang, L. Jiang and Q. Cheng, *ACS Nano*, 2014, **8**, 9511–9517.
23 J. Wang, Q. Cheng, L. Lin and L. Jiang, *ACS Nano*, 2014, **8**, 2739–2745.
24 B. Long, C. A. Wang, W. Lin, Y. Huang and J. Sun, *Compos. Sci. Technol.*, 2007, **67**, 2770–2774.
25 W. Lin, C. A. Wang, H. Le, B. Long and Y. Huang, *Mater. Sci. Eng., C*, 2008, **28**, 1031–1037.
26 T. H. Lin, W. H. Huang, I. K. Jun and P. Jiang, *Chem. Mater.*, 2009, **21**, 2039–2044.
27 C. A. Wang, Y. Huang, Q. Zan, H. Guo and S. Cai, *Mater. Sci. Eng., C*, 2000, **11**, 9–12.
28 D. X. Luong, A. K. Subramanian, G. A. L. Silva, J. Yoon, S. Cofer, K. Yang, P. S. Owuor, T. Wang, Z. Wang and J. Lou, *Adv. Mater.*, 2018, **30**, 1707416.
29 J. J. Martin, B. E. Fiore and R. M. Erb, *Nat. Commun.*, 2015, **6**, 8641.
30 S. Deville, E. Saiz and A. P. Tomsia, *Biomaterials*, 2017, **27**, 5480–5489.
31 Q. Cheng, C. Huang and A. P. Tomsia, *Adv. Mater.*, 2017, **29**, 1703155.
32 S. Deville, *Adv. Eng. Mater.*, 2010, **10**, 155–169.
33 E. Munch, E. Saiz, A. P. Tomsia and S. Deville, *J. Am. Ceram. Soc.*, 2009, **92**, 1534–1539.
34 S. Deville, E. Saiz, R. K. Nalla and A. P. Tomsia, *Science*, 2006, **311**, 515–518.
35 E. Munch, M. E. Launey, D. H. Alsem, E. Saiz, A. P. Tomsia and R. O. Ritchie, *Science*, 2008, **322**, 1516–1520.
36 H. Bai, Y. Chen, B. Delattre, A. P. Tomsia and R. O. Ritchie, *Sci. Adv.*, 2015, **1**, e1500849.
37 H. Bai, F. Walsh, B. Gludovatz, B. Delattre, C. Huang, Y. Chen, A. P. Tomsia and R. O. Ritchie, *Adv. Mater.*, 2016, **28**, 50–56.
38 H. Zhao, Y. Yue, L. Guo, J. Wu, Y. Zhang, X. Li, S. Mao and X. Han, *Adv. Mater.*, 2016, **28**, 5099–5105.
39 L. B. Mao, H. L. Gao, H. B. Yao, L. Liu, H. Cölfen, G. Liu, S. M. Chen, S. K. Li, Y. X. Yan and Y. Y. Liu, *Science*, 2016, **354**, 107–110.
40 Y. Cui, H. Gong, Y. Wang, D. Li and H. Bai, *Adv. Mater.*, 2018, **30**, e1706807.
41 Y. Si, X. Wang, L. Dou, J. Yu and B. Ding, *Sci. Adv.*, 2018, **4**, eaas8925.
42 C. Ferraro, E. Garcia-Tuñon, V. G. Rocha, S. Barg, M. D. Fariñas, T. E. G. Alvarez-Arenas, G. Sernicola, F. Giuliani and E. Saiz, *Adv. Funct. Mater.*, 2016, **26**, 1636–1645.
43 M. Yang, N. Zhao, Y. Cui, W. Gao, Q. Zhao, C. Gao, H. Bai and T. Xie, *ACS Nano*, 2017, **11**, 6817–6824.
44 E. D'Elia, S. Barg, N. Ni, V. G. Rocha and E. Saiz, *Adv. Mater.*, 2015, **27**, 4788–4794.
45 N. Zhao, M. Yang, Q. Zhao, W. Gao, T. Xie and H. Bai, *ACS Nano*, 2017, **11**, 4777–4784.
46 H. L. Gao, Y. B. Zhu, L. B. Mao, F. C. Wang, X. S. Luo, Y. Y. Liu, Y. Lu, Z. Pan, J. Ge and W. Shen, *Nat. Commun.*, 2016, **7**, 12920.

47 L. Qiu, J. Z. Liu, S. L. Y. Chang, Y. Wu and D. Li, *Nat. Commun.*, 2012, **3**, 1241.
48 O. T. Picot, V. G. Rocha, C. Ferraro, N. Ni, E. D'Elia, S. Meille, J. Chevalier, T. Saunders, T. Peijs and M. J. Reece, *Nat. Commun.*, 2017, **8**, 14425.
49 P. Zhang, J. Li, L. Lv, Y. Zhao and L. Qu, *ACS Nano*, 2017, **11**, 5087–5093.
50 N. Zheng, G. Fang, Z. Cao, Q. Zhao and T. Xie, *Polym. Chem.*, 2015, **6**, 3046–3053.
51 C. Wang, X. Chen, B. Wang, M. Huang, B. Wang, Y. Jiang and R. S. Ruoff, *ACS Nano*, 2018, **12**, 5816–5825.
52 H. Geng, X. Liu, G. Shi, G. Bai, J. Ma, J. Chen, Z. Wu, Y. Song, H. Fang and J. Wang, *Angew. Chem., Int. Ed.*, 2017, **56**, 997–1001.
53 X. Wang, J. Jin and M. Song, *Carbon*, 2013, **65**, 324–333.
54 Z. Li, R. Wang, R. J. Young, L. Deng, F. Yang, L. Hao, W. Jiao and W. Liu, *Polymer*, 2013, **54**, 6437–6446.
55 Y. J. Wan, L. X. Gong, L. C. Tang, L. B. Wu and J. X. Jiang, *Composites, Part A*, 2014, **64**, 79–89.
56 L. C. Tang, Y. J. Wan, D. Yan, Y. B. Pei, L. Zhao, Y. B. Li, L. B. Wu, J. X. Jiang and G. Q. Lai, *Carbon*, 2013, **60**, 16–27.
57 M. M. Shokrieh, S. M. Ghoreishi, M. Esmkhani and Z. Zhao, *Fatigue Fract. Eng. Mater. Struct.*, 2014, **37**, 1116–1123.
58 I. Zaman, T. T. Phan, H. C. Kuan, Q. Meng, L. T. Bao La, L. Luong, O. Youssf and J. Ma, *Polymer*, 2011, **52**, 1603–1611.
59 I. Zaman, H. C. Kuan, J. Dai, N. Kawashima, A. Michelmore, A. Sovi, S. Dong, L. Luong and J. Ma, *Nanoscale*, 2012, **4**, 4578–4586.
60 S. Chatterjee, J. W. Wang, W. S. Kuo, N. H. Tai, C. Salzmann, W. L. Li, R. Hollertz, F. A. Nüesch and B. T. T. Chu, *Chem. Phys. Lett.*, 2012, **531**, 6–10.
61 J. Jia, X. Sun, X. Lin, X. Shen, Y. W. Mai and J. K. Kim, *ACS Nano*, 2014, **8**, 5774–5783.
62 D. R. Bortz, C. Merino and I. Martin-Gullon, *Compos. Sci. Technol.*, 2011, **71**, 31–38.
63 W. Liu, Y. Wang, P. Wang, Y. Li, Q. Jiang, X. Hu, Y. Wei, Y. Qiu, S. I. S. Shahabadi and X. Lu, *Composites, Part B*, 2017, **113**, 197–205.
64 N. Lachman and H. D. Wagner, *Composites, Part A*, 2010, **41**, 1093–1098.
65 M. Wang, X. Fan, W. Thitsartarn and C. He, *Polymer*, 2015, **58**, 43–52.
66 I. Zaman, F. M. Nor, B. Manshoor, A. Khalid and S. Araby, *Procedia Manufacturing*, 2015, **2**, 23–27.
67 W. S. Hummers Jr and R. E. Offeman, *J. Am. Chem. Soc.*, 1958, **80**, 1339.
68 H. L. Gao, S. M. Chen, L. B. Mao, Z. Q. Song, H. B. Yao, H. Cölfen, X. S. Luo, F. Zhang, Z. Pan and Y. F. Meng, *Nat. Commun.*, 2017, **8**, 287.